

Antibody-Conjugated Signaling Nanocavities Fabricated by Dynamic Molding for Detecting Cancers Using Small Extracellular Vesicle Markers from Tears

Toshifumi Takeuchi,* Kisho Mori, Hirobumi Sunayama, Eri Takano, Yukiya Kitayama, Taku Shimizu, Yuzuki Hirose, Sachiko Inubushi, Ryohei Sasaki, and Hirokazu Tanino



Cite This: *J. Am. Chem. Soc.* 2020, 142, 6617–6624



Read Online

ACCESS |



Metrics & More

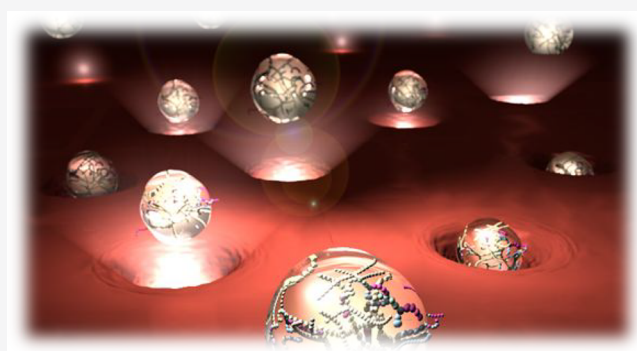


Article Recommendations



Supporting Information

ABSTRACT: Small extracellular vesicles (sEVs) are reliable biomarkers for early cancer detection; however, conventional detection methods such as immune-based assays and microRNA analyses are not very sensitive and require sample pretreatments and long analysis time. Here, we developed a molecular imprinting-based dynamic molding approach to fabricate antibody-conjugated signaling nanocavities capable of size recognition. This enabled the establishment of an easy-to-use, rapid, sensitive, pretreatment-free, and noninvasive sEV detection platform for efficient sEV detection-based cancer diagnosis. An apparent dissociation constant was estimated to be 2.4×10^{-16} M, which was ~ 1000 times higher than that of commercial immunoassays (analysis time, 5 min/sample). We successfully used tears for the first time to detect cancer-related intact sEVs, clearly differentiating between healthy donors and breast cancer patients, as well as between samples collected before and after total mastectomy. Our nanoprocessing strategy can be easily repurposed for the specific detection of other types of cancer by changing the conjugated antibodies, thereby facilitating the establishment of liquid biopsy for early cancer diagnosis.



INTRODUCTION

The crucial role of small extracellular vesicles (sEVs), nanosized extracellular vesicles, in the regulation of intercellular communication in multicellular organisms has been demonstrated recently.^{1,2} In addition, distinct sEVs have been attributed with specific functions in various processes, such as angiogenesis,^{3–7} epithelial–mesenchymal transition,⁸ chemoresistance,⁹ immune system avoidance,⁴ and cancer migration, invasion, and metastasis,^{4,10–14} in cancer tissues. These cancer-related sEVs have garnered increasing attention owing to their potential clinical applications.¹⁵

Early stage detection of cancers is vital for improving cancer survival and recovery rate and for avoiding recurrence in cancer patients. sEVs have been reported as promising biomarkers for liquid biopsy to easily predict the aggressiveness of developing cancers at an early stage.¹⁶ Therefore, significant efforts have been devoted to developing highly sensitive methods for detecting sEVs. Currently, the detection and characterization of sEVs in vivo require invasive collection of blood samples, and microRNAs (miRNAs) and proteins embedded inside and/or outside sEVs are analyzed by established methods such as real-time PCR, enzyme-linked immunosorbent assay (ELISA), Western blotting, and mass spectroscopy. These analytical methods usually involve time-consuming and tedious

pretreatments, such as ultracentrifugation and/or size-exclusion chromatography. Instead, a noninvasive, rapid, and sensitive platform that does not require sample pretreatment would be more convenient for patients and improve the examination rate for cancer screening, facilitating early detection of small cancers.

To avoid long analysis time, the detection of intact sEVs is more advantageous than the analysis of extracted miRNA and internal proteins inside sEVs. As sEVs embed membrane proteins on their surface, which originate from donor cells, the development of highly sensitive, selective, noninvasive, and pretreatment-free approaches for detecting the distinct membrane proteins on cancer cell-secreted sEVs could be a challenge when establishing an unprecedented method for rapid screening and precise detection of small cancers at an early stage.

Received: December 26, 2019

Published: March 10, 2020



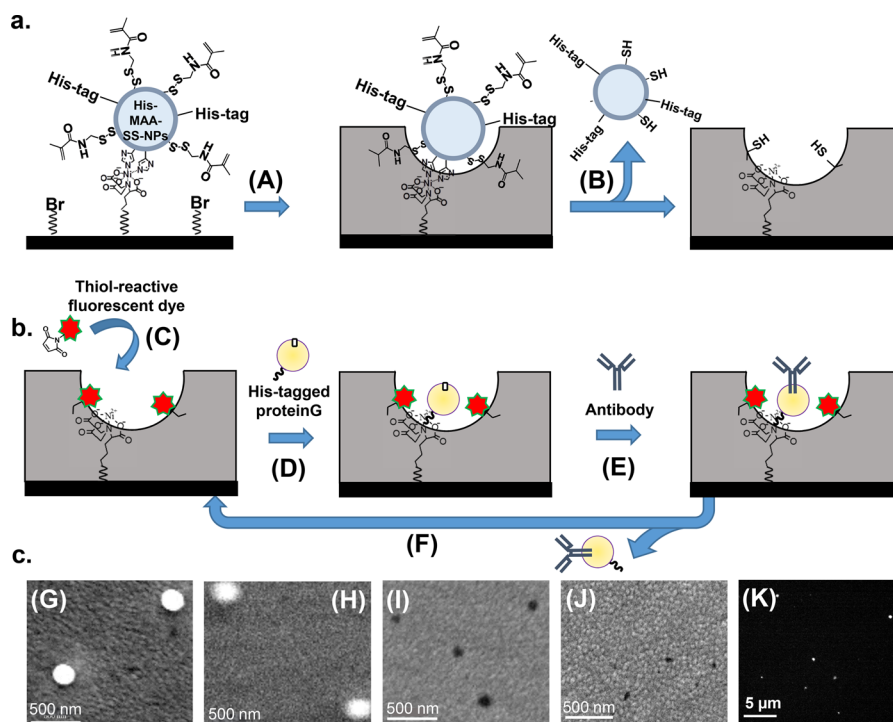


Figure 1. Antibody-conjugated signaling nanocavities for sensing intact small extracellular vesicles (sEVs) fabricated by molecular imprinting-based dynamic molding chemical nanoprocessing. a. Dynamic molding nanoprocessing. (A) Immobilization of methacrylamide-coupled His-tagged silica NPs (His-MAA-SS-NPs) as dynamic molds via coordination bonding with Ni(II)-coordinated nitrilotriacetic acid (Ni-NTA) on the substrate, and surface-initiated atom transfer radical polymerization (SI-ATRP) of 2-methacryloyloxyethyl phosphorylcholine (MPC) to form a biocompatible polymer matrix. (B) Removal of His-SH-NPs by ligand exchange of the Ni(II) complexes and reduction of the disulfide bonds to yield sEV-binding cavities. b. Postchemical nanoprocessing. (C) Introduction of a thiol-reactive fluorescent dye as a reporter molecule. (D) Introduction of His-tagged protein G via coordination bonding with Ni-NTA. (E) Oriented conjugation of desirable antibody via protein G. (F) Regeneration of sEV-binding cavities. c. Scanning electron microscopic (G–J) and fluorescence (K) images during the dynamic molding nanoprocessing approach. (G) Immobilized His-MAA-SS-NPs before ATRP. (H) Immobilized His-MAA-SS-NPs after SI-ATRP. (I) Nanocavities after removing His-tagged silica NPs bearing free SH groups (His-SH-NPs, 200 nm) by reduction. Average cavity size: 102.6 ± 33.7 nm ($n = 275$) from SEM images. (J) Nanocavities after removing His-SH-NPs (50 nm) by reduction. Average cavity size: 46.5 ± 12.5 nm ($n = 20$) from SEM images. (K) Fluorescence microscopic image of the nanoprocesed substrate after the introduction of a thiol-reactive fluorescent reporter molecule, AlexaFluor 647, fabricated using 200 nm His-MAA-SS-NPs as the dynamic mold.

Tears have been reported to contain sEVs,¹⁷ and they can be collected easily and noninvasively using the Schirmer tear test strip. Although cancer diagnosis using tear sEVs has not yet been reported, we believe that diagnosis using tears could be convenient for patients as tear drops can be self-collected by the Schirmer tear test strip at a hospital or at home. Therefore, in the current study, we have developed a noninvasive, rapid, and sensitive platform for sensing intact sEVs in tears with pretreatment-free and smooth operation, possessing comparable or even better sensitivity than that of previously reported methods.

Here, we report the efficiency of antibody-conjugated signaling nanocavities as a highly selective and sensitive platform for the detection of sEVs (Figure 1a,b). The nanocavities were prepared on a substrate with a newly developed chemical nanoprocessing approach involving dynamical molding, inspired by molecular imprinting,^{18–20} yielding sEV-sensing chips. The key feature of this strategy is the use of silica nanoparticles (NPs) as a dynamic mold to engineer nanocavities of transcribable sizes and the use of transplantable functional groups. Finally, the feasibility and reliability of the sEV-sensing chips for the noninvasive detection of breast cancer were demonstrated by analyzing sEVs in tear drops collected from breast cancer patients.

RESULTS AND DISCUSSION

Nanoimprint lithography is a cost-effective technique and a quick alternative to electron-beam lithography and extreme ultraviolet lithography. However, the chemical nanoprocessing technique employed in this study is simpler to perform than nanoimprint lithography (Figure 1a) because it has the advantage of dynamic molding, as opposed to precisely fabricated molds with fixed surface features, which are commonly used in nanolithography. For the fabrication of sEV-binding nanocavities, we used 50–200 nm silica NPs conjugated to hexahistidine peptide chains (His-tag) and free thiol groups (His-SH-NPs) as dynamic molds. First, His-SH-NPs were immobilized on a gold-coated glass substrate that was previously grafted with Ni(II)-coordinated nitrilotriacetic acid (Ni-NTA) and bromo (Br) groups, which acted as initiators for surface-initiated atom transfer radical polymerization (SI-ATRP). Coordination of His-tag with Ni-NTA immobilizes the His-SH-NPs on the substrate (Figure 1a). Then, the thiol groups on the His-SH-NPs were coupled with methacrylic acid by a disulfide exchange reaction with 2-(2-pyridyl)dithioethyl methacrylamide to yield methacrylamide-coupled His-tagged silica NPs (His-MAA-SS-NPs) (Figure 1a and Figure 1c–G). This enabled them to be copolymerized with the polymer matrix. Subsequently, SI-ATRP was

performed to form a layer of 2-methacryloyloxyethyl phosphorylcholine (MPC)-based biocompatible polymer matrix. This coating was intended to minimize off-target proteins from their nonspecific binding on the substrate²¹ (Figure 1a-A and c-H). SI-ATRP proceeded proportionally with polymerization time and the polymer matrix layer.

The immobilized silica NPs were then removed by diluted acetic acid and reduction of the disulfide bonds, which resulted in nanocavities depending upon the size of His-SH-NPs used (Figure 1a-B). To confirm the formation of nanocavities by removing the dynamic mold silica NPs (200 nm), the nanoprocessed substrate was examined by scanning electron microscopy (SEM; Figure 1c-I, J). The average size of the nanocavities was 102.6 ± 33.7 nm ($n = 275$; Figure 1c-I), with a density of 6×10^5 nanocavities/mm², which is 10 times higher than that fabricated by molecular imprinting using sEVs themselves as the template (5×10^4 nanocavities/mm², Figure S1). When 50 nm silica NPs were used as the dynamic mold, much smaller nanocavities, 46.5 ± 12.5 nm ($n = 20$; Figure 1c-J), were formed, implying that the surface was successfully engineered by the proposed dynamic molding-based nanoprocessing technique. To estimate the nanocavity-forming efficiency (ratio of the remaining silica NPs after polymerization to the initially immobilized silica NPs on a substrate), fluorescent dye (rhodamine)-labeled His-SH-NPs were used. The efficiency of nanocavity formation was found to be $61.0\% \pm 13.3\%$ ($n = 3$), which was estimated from the fluorescence intensities of the remaining silica NPs after ATRP (71.3 ± 3.74) divided by that before ATRP (116.8 ± 7.24). The subsequent removal ratio of the silica NPs was $96.7\% \pm 3.4\%$ ($n = 3$), which was estimated from the fluorescence intensities of the remaining silica NPs after the removal step (2.45 ± 0.83) divided by that of the remaining silica NPs after ATRP.

The role of His-MAA-SS-NPs is not only to act as a dynamic mold but also to deliver thiol groups and graft them on the inner walls of nanocavities during polymerization. Following the removal of His-MAA-SS-NPs by reductive cleavage of disulfide linkages, free thiol groups are left behind. It should be noted that the free thiol groups are present only inside the nanocavities as only the thiol source was the dynamic mold (i.e., His-MAA-SS-NPs). These thiol groups inside the nanocavities were later used for postchemical nanoprocessing to introduce a thiol-reactive fluorescent reporter molecule capable of signaling function for transducing binding events into fluorescence change (Figure 1b-C). The postchemical nanoprocessing labeling of the nanocavities with a fluorescent reporter was confirmed by the appearance of fluorescent spots in the micrographs, wherein the spots were observed due to halation, although the actual sizes were smaller than the diffraction-limited spatial resolution of the microscope used. As shown in Figure 1c-K, almost no fluorescence was observed outside the nanocavities. These results confirmed that the nanocavity-focused postchemical nanoprocessing resulted in the implantation of reporter fluorescent dyes within the nanocavity, as evident from almost no fluorescence background in the polymer matrix outside the nanocavities, indicating a remarkably improved signal-to-noise ratio, since the dense fluorescent reporter molecules inside the nanocavities also reportedly improve the sensitivity.²²

Easily exchangeable antibody conjugation is essential to facilitate the construction of differential antibody arrays. Herein, His-tagged protein G was employed as a binder for antibodies, where the binding capability of protein G toward

the Fc domain of the antibody and the coordination capability of His-tag with Ni-NTA allowed us to immobilize the antibody orientationally within the nanocavity and to exchange them readily later (Figure 1b-D, E and F). Thus, only the Ni-NTA moieties inside the nanocavity could form Ni complexes with His-tagged protein G, as they were protected by the dynamic mold during SI-ATRP, preventing them from being buried by the MPC polymer matrix. To immobilize antibodies via His-tagged protein G, the nanoprocessed substrate was inserted into the custom-made flat-type pipet tip (Figure S2), which was designed not only for aspirating and charging His-tagged protein G and antibodies for antibody immobilization but also for aspirating the sEV sample and measuring fluorescence intensity on the sEV-sensing chip. All procedures were carried out automatically by a programmable liquid handling robot (System Instruments Co. Ltd., Tokyo, Japan), the operation of which was reported previously²³ (Figure S2). His-tagged protein G was introduced (Figure 1b-D) by aspirating protein G solution and washing with PBS. Then, antibodies to be tested were orientationally introduced (Figure 1b-E).

The nanocavity size dependency on the used dynamic molds bearing different sizes (50, 100, and 200 nm) was determined by examining the binding behavior of fluorescent His-SH-NPs ($\lambda_{\text{ex}} = 569$ nm, $\lambda_{\text{em}} = 585$ nm) of sizes 50, 100, and 200 nm toward the nanocavities without conjugating protein G or antibodies (Figure 2). The nanocavities prepared using 50 nm

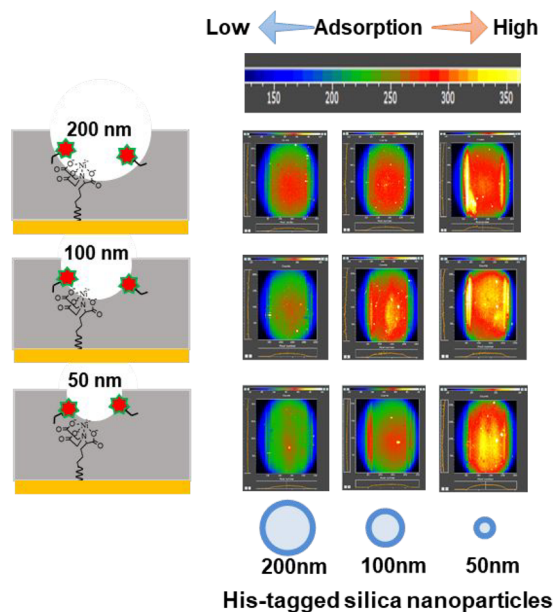


Figure 2. Nanocavity size dependency on the dynamic molds bearing different sizes: 200 nm (top), 100 nm (middle), and 50 nm (bottom), observed in the fluorescence images on the nanoprocessed chip. Heat map: yellow to red color indicates more adsorption of His-SH-NPs and green to blue color indicates less adsorption of His-SH-NPs.

His-MAA-SS-NPs mainly bound 50 nm fluorescent His-SH-NPs. With 100 nm His-MAA-SS-NPs, the resulting nanocavities bound both 50 and 100 nm fluorescent His-SH-NPs, but less binding of 200 nm fluorescent His-SH-NPs was observed. The nanocavities prepared using 200 nm His-MAA-SS-NPs bound all sizes of fluorescent His-SH-NPs. These results reveal that the nanocavity size can be controlled by changing the size of His-MAA-SS-NPs used in the dynamic

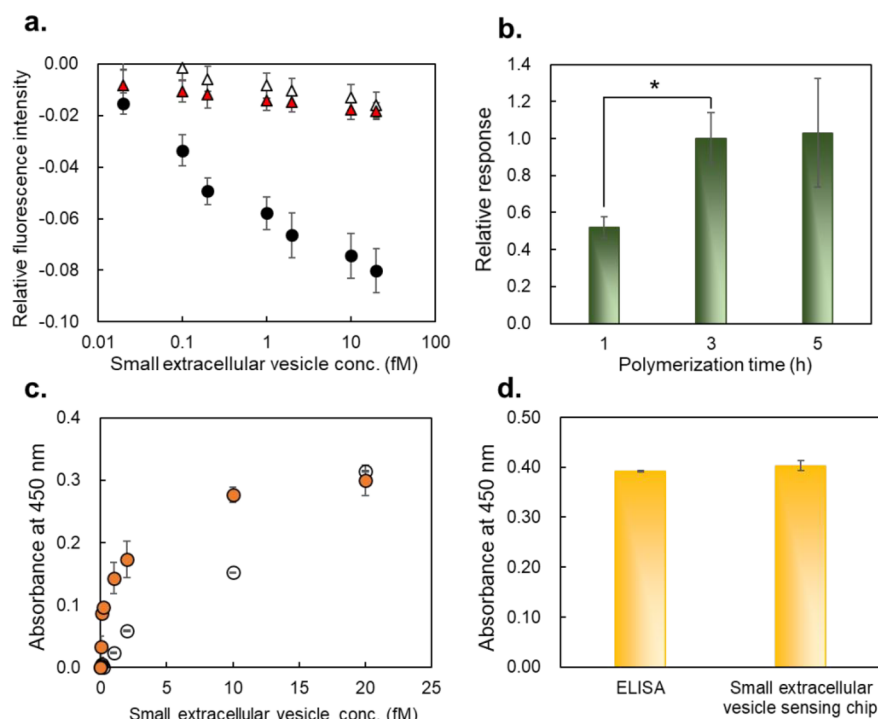


Figure 3. Performance of antibody-conjugated sEV-sensing chips. a. Fluorescence response of sEV-sensing chips conjugated with (black circle) and without (white triangle) the anti-CD9 antibody to PC3-secreted sEVs, and the response with free anti-CD9 antibody-treated sEVs (red triangle). The averages and standard deviations of the fluorescence intensities were calculated from the fluorescence intensities of three ROIs on three independent sEV-sensing chips ($n = 9$). b. Effect of polymer thickness on the relative response for PC3-secreted sEVs (1 fM, $n = 3$, *: $P < 0.05$). c. Sandwich assay for PC3-secreted sEVs on the commercially available ELISA plate (white circle) and the sEV-sensing chip (orange circle). d. Sandwich assay for the CD9/CD63 fusion protein (1.1 fM) on the commercially available ELISA plate and the sEV-sensing chip.

molding nanoprocessing approach. This presents an advantage over the previously proposed chemical nanoprocessing owing to the ability of size recognition and the simpler procedure. The previously reported sEV-imprinted method, in which polydisperse sEVs themselves are used as the template, results in the creation of nanocavities of heterogeneous sizes on a substrate, as is the case in conventional molecular imprinting.²⁴

As a model sEV, the PC3-secreted sEV was employed to examine the binding performance of the sEV-sensing chip, where the PC3 cell line was established from a human prostatic adenocarcinoma metastatic to bone with an average diameter of 80 nm (Figure S3). An antibody against CD9, a known sEV marker, was employed to fabricate a sEV-sensing chip. The fluorescence intensity on the chip was measured for various concentrations of PC3-secreted sEVs. The quantification was carried out using fluorescence images obtained by a CMOS camera equipped with a programmable liquid handling robot (Figure S2). The rapid detection of the sEVs, enabled by the use of an automated procedure, could achieve an analysis time of approximately 5 min/sample for the whole process, including aspiration of the sample, a 1 min incubation step, and transport of the chip to the insertion port to collect fluorescence images.

The fluorescence on the sEV-sensing chip was quenched as more PC3-secreted sEVs were added, and a linear relationship was observed in a semilogarithmic fashion from subfemtomolar to picomolar order (Figure 3a, black circle). Robust reproducibility of the raw fluorescence intensity data ($n = 9$) obtained from 1 fM sEV in 3 independent sEV-sensing chips with 3 region of interests (ROIs) on each chip was demonstrated (Table S1); the average raw fluorescence

intensity was 125.7 ± 2.2 [arbitrary unit]. The apparent dissociation constant (K_d) was estimated to be 2.4×10^{-16} M from the given binding isotherm using curve fitting based on 1:1 complex formation (Figure S4a), where the molar concentration of sEVs was calculated on a particle basis (1 mol = 6.02×10^{23} sEV particles). This value is lower than that of previously reported sEV-sensing chips prepared using sEVs themselves (6.0×10^{-16} M). The limit of detection was found to be 1.2×10^{-17} M with a $3S_D/m$ basis (m = slope of the linear part of the binding isotherm from 0 to 1.0×10^{-16} M, S_D = standard deviation for a value of 2.0×10^{-17} M sEVs), which implies that less than 10 sEVs/ μ L can be expected to be detected under the conditions employed. Strong binding behavior was not observed for PC3-secreted sEVs treated with free anti-CD9 antibodies, which would block the surface CD9 moiety, preventing interaction with the antibodies in the sensing nanocavities. (Figure 3a, red triangle). Furthermore, when the anti-CD9 antibodies were not introduced into the sEV-sensing nanocavities, almost no response was observed (Figure 3a, white triangle). These results confirmed the strong binding between the sEVs and the antibodies owing to the immobilization and attesting to the sensitivity of the nanocavity-specific introduction of the fluorescent reporter molecules.

The thickness of the MPC polymer matrix on the chip that was formed with SI-ATRP for 3 h was approximately 20 nm (Figure S5). When ATRP was carried out for 1 h, the response to 1 fM of PC3-secreted sEVs was reduced to about 50% compared with the 3 h polymerization chip, and when 5 h ATRP was conducted, the response was almost the same

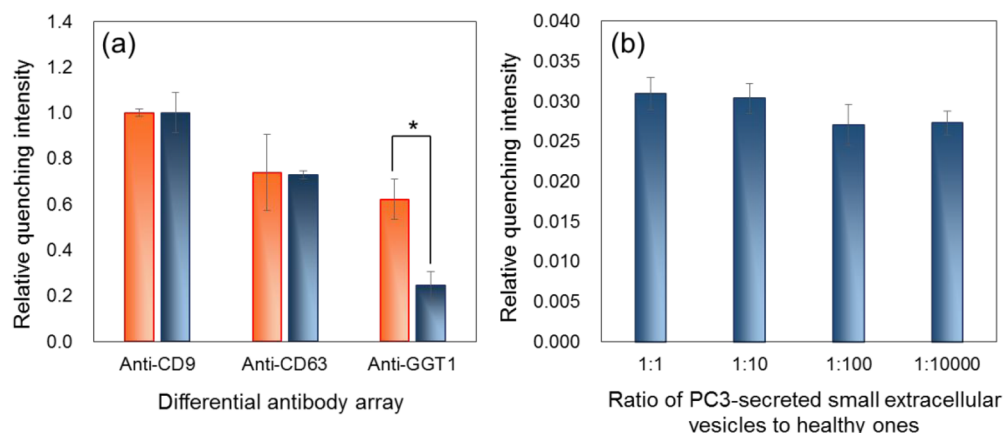


Figure 4. Binding behaviors of PC3-secreted sEVs and healthy sEVs. a. Binding of PC3-secreted sEVs (orange) and healthy sEVs (blue) to the sEV-sensing chip conjugated with anti-CD9, anti-CD63, or anti-GGT1 antibodies (1 fM, $n = 3$, *: $P < 0.05$). b. Effect of a large excess of healthy sEVs on the response of PC3-secreted sEVs (1 fM) to the anti-GGT1 antibody-conjugated sEV-sensing chip.

(Figure 3b). Therefore, we chose the 3 h ATRP conditions for subsequent experiments.

The apparent extremely high sensitivity of the sEV-sensing chip was comparable or even superior to previously reported pretreatment-free methods, such as nanoplasmonic biosensors,^{25,26} a miniaturized nuclear magnetic resonance system,²⁷ a sandwich assay-based 3D-nanopatterned microfluidic chip,²⁸ an electrogenerated chemiluminescence biosensor,²⁹ and a luminescent oxygen channeling immunoassay-based “ExoScreen” method.³⁰ This might be due to the sEV-sensing nanocavity presenting highly dense and oriented antibodies and a preferable round shape for sEV binding, enabling sEVs to form multipoint interactions with two or more anti-CD9 antibodies, thereby further stabilizing the interactions as the sEV occupies the nanocavity volume. Furthermore, antibodies and fluorescent reporter molecules can be introduced only inside the nanocavities, highly increasing the sensitivity.

To examine the effect of the sEV-sensing nanocavity with high antibody density on the sensitivity of sEV detection, a commercially available sandwich assay-based ELISA kit with a microplate immobilized with anti-CD9 antibodies and horseradish peroxidase (HRP)-labeled CD63 antibodies was used to detect PC3-secreted sEVs. The apparent K_d was estimated to be 1.2×10^{-13} M (Figure 3c-white circle, Figure S4b) in the conventional ELISA. Notably, the apparent K_d in our novel fluorescence detection method was approximately 1000 times higher than that of ELISA. Furthermore, the anti-CD9 antibody-conjugated sEV-sensing chip without fluorescence labeling (sandwich strategy) exhibited 100 times more sensitive detection of PC3-secreted sEVs than that of ELISA, where the apparent K_d was estimated to be 1.1×10^{-15} M (Figures 3c, orange circle, and S4c). From these results, the extremely high sensitivity may originate from the nanocavity effect and the specific in-nanocavity introduction of the fluorescent dye by the proposed molecular imprinting-based dynamic molding.

As shown in Figure 3d, the response to the CD9/CD63 fusion protein in the sandwich assay (1.1 fM) was almost the same on the ELISA plate and the sEV-sensing chip without fluorescence labeling. This suggests that the extremely high sensitivity was derived from multivalent interactions between antibodies and sEVs, which were facilitated by the nanocavity effect derived from the proposed dynamic molding chemical nanoprocessing. The specific in-nanocavity introduction of the

fluorescence dye also contributed to the decline of background, while nonspecific binding of the secondary antibody is inevitable in ELISA, increasing background noise.

Additional factors that could affect the sensitivity include the density on the sensing chip and the size homogeneity of the nanocavity. More stable and monodispersed His-MAA-SS-NPs could lead to higher density and a more homogeneous size of nanocavities, resulting in higher sensitivity. Furthermore, the postchemical nanoprocessing steps would be important for the sensitivity, and increasing the number of available free thiol groups and Ni-NTA in the nanocavity may provide brighter fluorescence from the nanocavity and denser antibody concentration inside the nanocavity, resulting in a higher signal-to-noise ratio and a stronger affinity based on more multipoint interactions, respectively.

Regarding analysis time, the fluorescence-based detection strategy required less detection time (within 5 min) than that of the ELISA-based strategy (approximately 2 h), suggesting that the nanocavity-specific introduction of fluorescent reporter molecules by the chemical nanoprocessing not only contributed to the development of a highly sensitive method but also a rapid and straightforward alternative.

Since characteristic membrane proteins, originating from the corresponding sEV-secreting cells, are present on the surface of sEVs, the discrimination of the composition of membrane proteins on intact sEVs between cancer-related sEVs and healthy ones could aid cancer detection. To facilitate the accuracy of cancer-related sEV detection, the “differential antibody array concept”³¹ was adopted, wherein sEV recognition depended on a pattern-based analysis method. For this, multiple sEV-sensing chips conjugated with different antibodies against diverse sEV-related membrane proteins were used. The fabrication of such sensor chips was easy, as it only required the introduction of His-tagged protein G, capable of binding the Fc region of antibodies before the immobilization of antibodies in the sEV-sensing nanocavity. We first ascertained the capability of the chips to distinguish the sEV markers CD9 and CD63, which are present on healthy sEVs, and γ -glutamyl transferase 1 (GGT1), a prostate cancer-related membrane protein present on PC3-secreted sEVs. Three independent sEV-sensing chips, each containing anti-CD9, anti-CD63, or anti-GGT1 antibodies, were prepared and used for the detection of PC3-secreted and healthy sEVs. The relative fluorescence intensities (ratio of a fluorescence

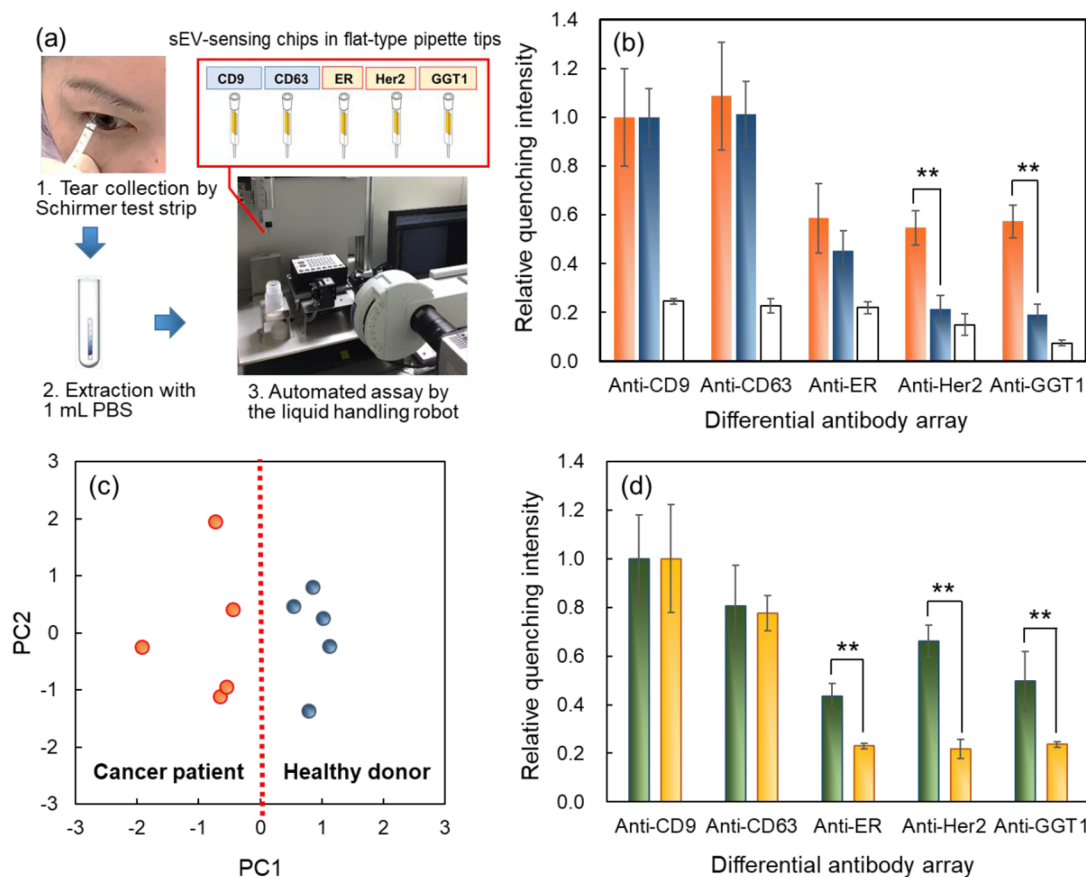


Figure 5. Detection of breast cancer-related sEVs in tears. a. Tear sEV detection procedure. b. Binding behavior of tear sEVs collected from breast cancer patients (orange) and healthy donors (blue; $n = 5$, **: $P < 0.005$). Ultracentrifuged tear samples (sEV-free) from healthy donors (100 000g, 4 °C, 12 h) are displayed in white. c. Pattern-based analysis by principal component analysis ($n = 5$). d. Binding behaviors of tear sEVs collected from breast cancer patients (stage I) before (green) and after (yellow) total mastectomy (**: $P < 0.005$).

intensity change, obtained from each sensor chip, to that from the anti-CD9 antibody-conjugated sensor chip) were plotted (Figure 4a). The response from PC3-secreted sEVs was higher than that from healthy sEVs with the anti-GGT1 antibody-conjugated sensor chip, whereas the anti-CD63 antibody-conjugated sensor chip showed almost no difference between PC3-secreted and healthy sEVs.

The effects of a large excess of healthy sEVs on the response of 1 fM of PC3-secreted sEVs were examined with the anti-GGT1-conjugated sEV-sensing chip. As shown in Figure 4b, negligible interference was observed with 10 000 times higher concentrations of healthy sEVs. From these results, we concluded that the sEV-sensing chips possess the potential for detecting cancer-related sEVs in a differential antibody array.

To assess the potential for detecting cancers, we studied the efficiency of the sEV sensor chips using body fluids collected from breast cancer patients and compared them with those from healthy volunteers. Informed consent from all participants was obtained per the guidelines of the ethics committees at Kobe University Hospital (#180195) and Graduate School of Engineering, Kobe University (#30-03). We chose tears as the test body fluid because tear drops can be more easily collected from breast cancer patients in a noninvasive manner than commonly used blood samples. To the best of our knowledge, no tear-based cancer detection assay has been reported so far. Tear drops from five breast cancer patients and five healthy female donors were collected using Schirmer tear

test strips as described previously.²⁴ The sEVs were extracted by incubation with 500–1000 μL of 10 mM phosphate buffer containing 140 mM NaCl (PBS).

The extracted tear sEVs were directly analyzed without any pretreatment such as ultracentrifugation or size-exclusion chromatography (Figure 5a), which ensured that those analyzed were intact sEVs with no interference from the off-target proteins present inside the sEVs. For constructing a differential antibody array for detecting breast cancer-related sEVs, five different antibodies—anti-CD9, anti-CD63, anti-estrogen receptor (ER), antihuman epidermal growth factor receptor 2 (Her2), or anti-GGT1—were conjugated on each sEV-sensing chip. From the obtained data (Figure 5b, orange bar is for breast cancer patients and blue bar is for healthy donors), pattern-based analysis was performed using principal component analysis. As shown in Figure 5c, the group of breast cancer patients was separated from the group of healthy volunteers. To confirm that the response originated from tear sEV, sEV-free tear samples were prepared by ultracentrifugation (100 000 g) of tear drops from healthy donors for 12 h at 4 °C (Figure 5b-white bar). The sEV-free samples showed almost no response, demonstrating that the sEV-sensing nanocavities successfully transduced sEV binding events into fluorescence change.

As another proof of concept, tears of a stage I breast cancer patient (ER+, Her2 score 1) before and after total mastectomy were analyzed. As can be seen in Figure 5d, responses to anti-ER antibodies and anti-Her2 antibodies decreased after the

surgery. These results clearly showed the possibility of detecting cancer-related sEVs and determining whether patients suffer from breast cancer. Thus, the present pretreatment-free sEV-sensing system promotes a new liquid biopsy tool for diagnosing breast cancer; however, further investigation is required to verify the accuracy of diagnosis by increasing the sample size and comparing results with the current gold standard, namely, mammography with echography.

CONCLUSION

In conclusion, we demonstrated that the antibody-conjugated nanocavity-based platform, fabricated by silica NP-based dynamic molding using a molecular imprinting approach, is a useful tool for rapidly sensing intact sEVs in biological fluids. In this study, we adopted a differential antibody array format and pattern-based analysis to validate the effectiveness of the sensor. Besides being a highly sensitive, rapid, and easy method for directly sensing sEVs, the tool can be customized to diagnose various cancers and infectious diseases by changing and optimizing dynamic molding sizes and antibodies. Thus, the proposed strategy could accelerate research on the important applications of extracellular vesicles, viruses, bacteria, and cells in diverse areas of life and medical sciences.

ASSOCIATED CONTENT

Supporting Information

The Supporting Information is available free of charge at <https://pubs.acs.org/doi/10.1021/jacs.9b13874>.

Detailed description of the experimental methods; including typical SEM images of the nanoprocessed substrates; the flat-type pipet tip, and the liquid handling robot with a fluorescence microscope unit; size-distribution of PC3-secreted sEV; estimation of dissociation constants (K_d); MPC polymer growth with the polymerization time; materials, apparatuses, preparation of 2-aminoethyl-2-pyridylsulfide, 2-(2-pyridyl)dithioethyl methacrylamide, and silica NPs bearing thiol groups and His-tag (His-SH-NPs); fabrication of antibody-conjugated sEV sensing chips; fluorescence detection of silica NPs on the substrate; fluorescence detection of sEVs on the sEV sensing chip; enzyme-linked immunosorbent assay; and collection of human tear drops (PDF)

AUTHOR INFORMATION

Corresponding Author

Toshifumi Takeuchi – Graduate School of Engineering and Medical Device Fabrication Engineering Center, Graduate School of Engineering, Kobe University, Kobe 657-8501, Japan; orcid.org/0000-0002-5641-2333; Email: takeuchi@gold.kobe-u.ac.jp

Authors

Kisho Mori – Graduate School of Engineering, Kobe University, Kobe 657-8501, Japan

Hirobumi Sunayama – Graduate School of Engineering, Kobe University, Kobe 657-8501, Japan; orcid.org/0000-0001-5145-2312

Eri Takano – Graduate School of Engineering, Kobe University, Kobe 657-8501, Japan; orcid.org/0000-0002-2931-4527

Yukiya Kitayama – Graduate School of Engineering and Medical Device Fabrication Engineering Center, Graduate School of Engineering, Kobe University, Kobe 657-8501, Japan; orcid.org/0000-0002-7418-301X

Taku Shimizu – Graduate School of Engineering, Kobe University, Kobe 657-8501, Japan

Yuzuki Hirose – Graduate School of Engineering, Kobe University, Kobe 657-8501, Japan

Sachiko Inubushi – Division of Radiation Oncology, Kobe University Hospital, Kobe 650-0017, Japan

Ryohei Sasaki – Division of Radiation Oncology, Kobe University Hospital, Kobe 650-0017, Japan; Medical Device Fabrication Engineering Center, Graduate School of Engineering, Kobe University, Kobe 657-8501, Japan; orcid.org/0000-0002-4994-9386

Hirokazu Tanino – Department of Breast and Endocrine Surgery, Kobe University Hospital, Kobe 650-0017, Japan

Complete contact information is available at:

<https://pubs.acs.org/10.1021/jacs.9b13874>

Notes

The authors declare no competing financial interest.

ACKNOWLEDGMENTS

This work was supported by JSPS KAKENHI (JP19H00854 and JP16H06280), the Cooperative Research Program of “Network Joint Research Center for Materials and Devices”, and the Foundation for Biomedical Research and Innovation at Kobe. We thank the late Professor Isao Karube, President at Tokyo University of Technology (Japan) for his valuable suggestion.

REFERENCES

- (1) Valadi, H.; Ekström, K.; Bossios, A.; Sjöstrand, M.; Lee, J. J.; Lötvall, J. O. Exosome-mediated transfer of mRNAs and microRNAs is a novel mechanism of genetic exchange between cells. *Nat. Cell Biol.* **2007**, *9*, 654–659.
- (2) Hoshino, A.; Costa-Silva, B.; Shen, T.-L.; Rodrigues, G.; Hashimoto, A.; Tesic Mark, M.; Molina, H.; Kohsaka, S.; Di Giannatale, A.; Ceder, S.; Singh, S.; Williams, C.; Soplol, N.; Uryu, K.; Pharmed, L.; King, T.; Bojmar, L.; Davies, A. E.; Ararso, Y.; Zhang, T.; Zhang, H.; Hernandez, J.; Weiss, J. M.; Dumont-Cole, V. D.; Kramer, K.; Wexler, L. H.; Narendran, A.; Schwartz, G. K.; Healey, J. H.; Sandstrom, P.; Jørgen Labori, K.; Kure, E. H.; Grandgenett, P. M.; Hollingsworth, M. A.; de Sousa, M.; Kaur, S.; Jain, M.; Mallya, K.; Batra, S. K.; Jarnagin, W. R.; Brady, M. S.; Fodstad, O.; Muller, V.; Pantel, K.; Minn, A. J.; Bissell, M. J.; Garcia, B. A.; Kang, Y.; Rajasekhar, V. K.; Ghajar, C. M.; Matei, I.; Peinado, H.; Bromberg, J.; Lyden, D. Tumour exosome integrins determine organotropic metastasis. *Nature* **2015**, *527*, 329–335.
- (3) Tadokoro, H.; Umezumi, T.; Ohyashiki, K.; Hirano, T.; Ohyashiki, J. H. Exosomes derived from hypoxic leukemia cells enhance tube formation in endothelial cells. *J. Biol. Chem.* **2013**, *288*, 34343–34351.
- (4) Ye, S. B.; Li, Z. L.; Luo, D. H.; Huang, B. J.; Chen, Y. S.; Zhang, X. S.; Cui, J.; Zeng, Y. X.; Li, J. Tumor-derived exosomes promote tumor progression and T-cell dysfunction through the regulation of enriched exosomal microRNAs in human nasopharyngeal carcinoma. *Oncotarget* **2014**, *5*, 5439–5452.
- (5) Zhuang, G.; Wu, X.; Jiang, Z.; Kasman, I.; Yao, J.; Guan, Y.; Oeh, J.; Modrusan, Z.; Bais, C.; Sampath, D.; Ferrara, N. Tumour-secreted miR-9 promotes endothelial cell migration and angiogenesis by activating the JAK-STAT pathway. *EMBO J.* **2012**, *31*, 3513–3523.
- (6) Umezumi, T.; Ohyashiki, K.; Kuroda, M.; Ohyashiki, J. H. Leukemia cell to endothelial cell communication via exosomal miRNAs. *Oncogene* **2013**, *32*, 2747–2755.

- (7) Umezu, T.; Tadokoro, H.; Azuma, K.; Yoshizawa, S.; Ohyashiki, K.; Ohyashiki, J. H. Exosomal miR-135b shed from hypoxic multiple myeloma cells enhances angiogenesis by targeting factor-inhibiting HIF-1. *Blood* **2014**, *124*, 3748–3757.
- (8) Melo, S. A.; Sugimoto, H.; O'Connell, J. T.; Kato, N.; Villanueva, A.; Vidal, A.; Qiu, L.; Vitkin, E.; Perelman, L. T.; Melo, C. A.; Lucci, A.; Ivan, C.; Calin, G. A.; Kalluri, R. Cancer exosomes perform cell-independent microRNA biogenesis and promote tumorigenesis. *Cancer Cell* **2014**, *26*, 707–721.
- (9) Chen, W. X.; Liu, X. M.; Lv, M. M.; Chen, L.; Zhao, J. H.; Zhong, S. L.; Ji, M. H.; Hu, Q.; Luo, Z.; Wu, J. Z.; Tang, J. H. Exosomes from drug-resistant breast cancer cells transmit chemoresistance by a horizontal transfer of microRNAs. *PLoS One* **2014**, *9*, No. e95240.
- (10) Singh, R.; Pochampally, R.; Watabe, K.; Lu, Z.; Mo, Y. Y. Exosome-mediated transfer of miR-10b promotes cell invasion in breast cancer. *Mol. Cancer* **2014**, *13*, 256.
- (11) Yang, M.; Chen, J.; Su, F.; Yu, B.; Su, F.; Lin, L.; Liu, Y.; Huang, J. D.; Song, E. Microvesicles secreted by macrophages shuttle invasion-potentiating microRNAs into breast cancer cells. *Mol. Cancer* **2011**, *10*, 117.
- (12) Kogure, T.; Lin, W. L.; Yan, I. K.; Braconi, C.; Patel, T. Intercellular nanovesicle-mediated microRNA transfer: A mechanism of environmental modulation of hepatocellular cancer cell growth. *Hepatology* **2011**, *54*, 1237–1248.
- (13) Fabbri, M.; Paone, A.; Calore, F.; Galli, R.; Gaudio, E.; Santhanam, R.; Lovat, F.; Fadda, P.; Mao, C.; Nuovo, G. J.; Zanesi, N.; Crawford, M.; Ozer, G. H.; Wernicke, D.; Alder, H.; Caligiuri, M. A.; Nana-Sinkam, P.; Perrotti, D.; Croce, C. M. MicroRNAs bind to Toll-like receptors to induce prometastatic inflammatory response. *Proc. Natl. Acad. Sci. U. S. A.* **2012**, *109*, E2110–E2116.
- (14) Ostenfeld, M. S.; Jeppesen, D. K.; Laurberg, J. R.; Boysen, A. T.; Bramsen, J. B.; Prindal-Bengtson, B.; Hendrix, A.; Lamy, P.; Dagnaes-Hansen, F.; Rasmussen, M. H.; Bui, K. H.; Fristrup, N.; Christensen, E. I.; Nordentoft, I.; Morth, J. P.; Jensen, J. B.; Pedersen, J. S.; Beck, M.; Theodorescu, D.; Borre, M.; Howard, K. A.; Dyrskjot, L.; Orntoft, T. F. Cellular disposal of miR23b by RAB27-dependent exosome release is linked to acquisition of metastatic properties. *Cancer Res.* **2014**, *74*, 5758–5771.
- (15) Siravegna, G.; Marsoni, S.; Siena, S.; Bardelli, A. Integrating liquid biopsies into the management of cancer. *Nat. Rev. Clin. Oncol.* **2017**, *14*, 531–548.
- (16) Théry, C. Diagnosis by extracellular vesicles. *Nature* **2015**, *523*, 161–162.
- (17) Aqrawi, L. A.; Galtung, H. K.; Vestad, B.; Øvstebø, R.; Thiede, B.; Rusthen, S.; Young, A.; Guerreiro, E. M.; Utheim, T. P.; Chen, X.; Utheim, Ø. A.; Palm, Ø.; Jensen, J. L. Identification of potential saliva and tear biomarkers in primary Sjögren's syndrome, utilising the extraction of extracellular vesicles and proteomics analysis. *Arthritis Res. Ther.* **2017**, *19*, 14.
- (18) Takeuchi, T.; Sunayama, H. Beyond natural antibodies. a new generation of synthetic antibodies created by post-imprinting modification of molecularly imprinted polymer. *Chem. Commun.* **2018**, *54*, 6243–6251.
- (19) Komiyama, M.; Mori, T.; Ariga, K. Molecular Imprinting: Materials Nanoarchitectonics with Molecular Information. *Bull. Chem. Soc. Jpn.* **2018**, *91*, 1075–1111.
- (20) Takeuchi, T.; Hayashi, T.; Ichikawa, S.; Kaji, A.; Masui, M.; Matsumoto, H.; Sasao, R. Molecularly imprinted tailor-made functional polymer receptors for highly sensitive and selective separation and detection of target molecules. *Chromatography* **2016**, *37*, 43–64.
- (21) Ishihara, K.; Ueda, T.; Nakabayashi, N. Preparation of phospholipid polymers and their properties as polymer hydrogel membranes. *Polym. J.* **1990**, *22*, 355–360.
- (22) Horikawa, R.; Sunayama, H.; Kitayama, Y.; Takano, E.; Takeuchi, T. Programmable signaling molecular recognition nanocavity prepared by molecular imprinting and post-imprinting modifications. *Angew. Chem., Int. Ed.* **2016**, *55*, 13023–13027.
- (23) Takano, E.; Shimura, N.; Ujima, Y.; Sunayama, H.; Kitayama, Y.; Takeuchi, T. Highly sensitive fluoro-immunosensing for biomarker detection using an automatic pipette tip-type biosensing system. *ACS Omega* **2019**, *4*, 1487–1493.
- (24) Mori, K.; Hirase, M.; Morishige, T.; Takano, E.; Sunayama, H.; Kitayama, Y.; Inubushi, S.; Sasaki, R.; Yashiro, M.; Takeuchi, T. A Pretreatment-Free, Polymer-Based Platform Prepared by Molecular Imprinting and Post-Imprinting Modifications for Sensing Intact Exosomes. *Angew. Chem., Int. Ed.* **2019**, *58*, 1612–1615.
- (25) Im, H.; Shao, H.; Park, Y. I.; Peterson, V. M.; Castro, C. M.; Weissleder, R.; Lee, H. Label-free detection and molecular profiling of exosomes with a nano-plasmonic sensor. *Nat. Biotechnol.* **2014**, *32*, 490–495.
- (26) Qiu, G.; Thakur, A.; Xu, C.; Ng, S.-P.; Lee, Y.; Wu, C.-M. L. Detection of glioma-derived exosomes with the biotinylated antibody-functionalized titanium nitride plasmonic biosensor. *Adv. Funct. Mater.* **2019**, *29*, 1806761.
- (27) Shao, H.; Chung, J.; Balaj, L.; Charest, A.; Bigner, D. D.; Carter, B. S.; Hochberg, F. H.; Breakefield, X. O.; Weissleder, R.; Lee, H. Protein typing of circulating microvesicles allows real-time monitoring of glioblastoma therapy. *Nat. Med.* **2012**, *18*, 1835–40.
- (28) Zhang, P.; Zhou, X.; He, M.; Shang, Y.; Tetlow, A. L.; Godwin, A. K.; Zeng, Y. Ultrasensitive detection of circulating exosomes with a 3D-nanopatterned microfluidic chip. *Nat. Biomed. Eng.* **2019**, *3*, 438–451.
- (29) Zhang, Y.; Wang, F.; Zhang, H.; Wang, H.; Liu, Y. Multivalency interface and g-C₃N₄ coated liquid metal nanoprobe signal amplification for sensitive electrogenerated chemiluminescence detection of exosomes and their surface proteins. *Anal. Chem.* **2019**, *91* (18), 12100–12107.
- (30) Yoshioka, Y.; Kosaka, N.; Konishi, Y.; Ohta, H.; Okamoto, H.; Sonoda, H.; Nonaka, R.; Yamamoto, H.; Ishii, H.; Mori, M.; Furuta, K.; Nakajima, T.; Hayashi, H.; Sugisaki, H.; Higashimoto, H.; Kato, T.; Takeshita, F.; Ochiya, T. Ultra-sensitive liquid biopsy of circulating extracellular vesicles using ExoScreen. *Nat. Commun.* **2014**, *5*, 3591.
- (31) Wright, A. T.; Anslyn, E. V. Differential receptor arrays and assays for solution-based molecular recognition. *Chem. Soc. Rev.* **2006**, *35*, 14–28.